Sustainable Fuels from CO_2-rich synthesis gas via Fischer-Tropsch technology

Bart C.A. de Jong[1], Konstantijn T. Rommens[2], Tal Rosner[3], Paul van den Tempel[4], Léon Rohrbach[1], G. Leendert Bezemer[5], Hero J. Heeres[1], Mark Saeys[2], Charlotte Vogt[6] and Jingxiu Xie[1,]*

[1] Green Chemical Reaction Engineering, Engineering & Technology Institute Groningen, University of Groningen, Nijenborgh 3, 9747 AG Groningen, The Netherlands

[2] Laboratory for Chemical Technology (LCT), Department of Materials, Textiles and Chemical Engineering, Ghent University, Technologiepark 125, 9052, Ghent, Belgium

[3] Schulich Faculty of Chemistry, and Russel Berri Nanoscience and Nanotechnology Institute, Technion - Israel Institute of Technology, Technion City, Haifa 32000, Israel

[4] Product Technology, Engineering & Technology Institute Groningen, University of Groningen, Nijenborgh 3, 9747 AG Groningen, The Netherlands

[5] Energy Transition Campus Amsterdam, Shell Global Solutions International B.V., Grasweg 31, 1031 HW Amsterdam, The Netherlands

[6] Schulich Faculty of Chemistry, and Resnick Sustainability Center for Catalysis, Technion - Israel Institute of Technology, Technion City, Haifa 32000, Israel

KEYWORDS

Carbon dioxide, Synthesis gas, Mixed feeds, Synthetic fuels, Fischer-Tropsch, Methanation, Cobalt

ABSTRACT

CO_2-containing synthesis gas is a relevant feedstock for the production of synthetic fuels using Fischer-Tropsch Synthesis. We report the role of CO_2 in CO_2, CO and H_2 mixed feeds over a cobalt-based catalyst at 220 °C and 21 bar in a packed bed reactor. The C_{5+} selectivity remains above 78 % even for CO_2-rich synthesis gas with 75 % $CO_2/(CO+CO_2)$. Using $^{13}CO_2$ isotopic labeling, the increase in methane selectivity is attributed to both CO and CO_2 methanation, which is limited by maintaining a H_2/CO outlet ratio below 10 and an outlet CO partial pressure above 0.2 bar, respectively. Operando modulated DRIFTS confirms a positive relationship between CO surface coverage and CO partial pressure. From DFT and microkinetic modeling, enhanced CO and CO_2 methanation could be attributed to a lower CO surface coverage and a higher H_2 surface coverage. This work identifies boundaries for efficient cobalt-catalyzed mixed-feed FTS for synthetic fuels production.

1. Introduction

The aviation sector currently accounts for 2.4 % of global CO_2 emissions, a share likely to increase as aviation fuel cannot effectively be replaced in the near future with H_2 or batteries [1–3]. To reduce the climate impact of the aviation sector, sustainable aviation fuel (SAF) is produced from renewable H_2 and alternative carbon feedstocks, such as municipal waste, biomass, and CO/CO_2-containing waste gas streams, via Fischer-Tropsch Synthesis (FTS) [1,4]. FTS converts synthesis gas (syngas), a mixture of CO and H_2, into a range of hydrocarbons [5–7]. These hydrocarbons can be converted into SAF, which has superior combustion properties compared to conventional aviation fuels [8]. Figure 1a presents the general process flowsheet for producing synthetic kerosene via the Gas-to-Liquids (GTL) and the Power-to-Liquids (PTL) technology. [9–12]. In the GTL technology, synthesis gas is produced from natural gas via partial oxidation of methane (POM) or methane reforming (MR) and converted into hydrocarbons via FTS (Figure 1a) [13]. The hydrocarbon products are then isomerized, hydrocracked and upgraded into SAF. In the PTL route, CO_2 and green H_2 are used for the SAF production (Figure 1a) [14,15]. The synthesis gas production proceeds via the reverse water gas shift (RWGS) reaction, followed by the same steps as GTL.

To evaluate syngas production via RWGS, its equilibrium between CO and CO_2 versus temperature is presented in Figure 1b. Higher temperatures favor this endothermic reaction. A higher H_2/CO_2 feed ratio increases equilibrium conversion but also raises the output H_2/CO ratio. In the industrially relevant temperature range of 600 to 800 °C, the RWGS unit outlet has a CO_2 fraction (fraction $CO_2/(CO+CO_2)$) of 20-50 % CO_2. In alternative feeds such as CO-rich emission gas from the steel and cement industries, CO_2 is also present in significant amounts [16]. Therefore, either a CO_2 scrubber is required, or CO_2 needs to be tolerated in the FTS unit. CO_2 could

potentially replace other inert gases that have been proposed to be added to improve the process for enhanced heat transfer and dilution of the partial pressure of water that is formed [17–19].

FTS is catalyzed by iron or cobalt-based catalysts [5,6]. As metallic cobalt-based catalysts are inactive for RWGS and operate at lower temperatures, they produce mainly paraffinic C_{5+}-hydrocarbons which is ideal for synthetic kerosene [8,20]. FTS with a pure CO and H_2 feed has extensively been researched, and also the methanation activity for CO_2 hydrogenation over cobalt-based catalysts is well established [5,6,21,22]. However, there are dissenting opinions on the role of CO_2 in mixed-feed streams where some groups mentioned that CO_2 acts as inert gas, while other groups reported conversion of CO_2 into methane [23–34]. Riedel et al. studied mixed-feed FTS at 190 °C and 10 bar using a Co/Mn/Aerosil/Pt catalyst and found that CO_2 acts as diluent until CO_2 fraction was above 75 %, when CO_2 methanation commenced [27]. Yao et al. used a Co/TiO_2 catalyst at 200 °C and 21 bar and found that for CO_2 fractions above 50 %, CO_2 was converted to methane [28]. Using isotopic labelled $^{14}CO_2$ in a mixed-feed at 220 °C and 20 bar over a $Co/Pt/Al_2O_3$ catalyst, the Davis group concluded that CO_2 methanation occurred even at CO_2 fractions below 50 % [29].

In this study, we define the process boundary conditions where CO_2 switches from an inert to a reactive gas in FTS using an industrially relevant titania-supported metallic cobalt catalyst loaded in a packed-bed reactor operating at 220 °C and 21 bar. These boundaries allow for operation of mixed-feed FTS where CO_2 and H_2 are not converted in undesired methane. We hypothesize that the conversion level, H_2/CO ratios, and H_2 partial pressure should all be well-defined to establish clear experimental boundary conditions [23–34]. To align the H_2/CO_x ratio of the RWGS effluent with the FTS feed, the H_2/CO_x ratio was fixed at 2 [35]. Upon identifying boundary conditions where CO_2 co-feeding increased methane selectivity and descriptors thereof, *in-situ* DRIFTS, isotopic

labelling experiments, and microkinetic modeling were employed to unravel the molecular origin of increased methane production and limited CO_2 reactivity.

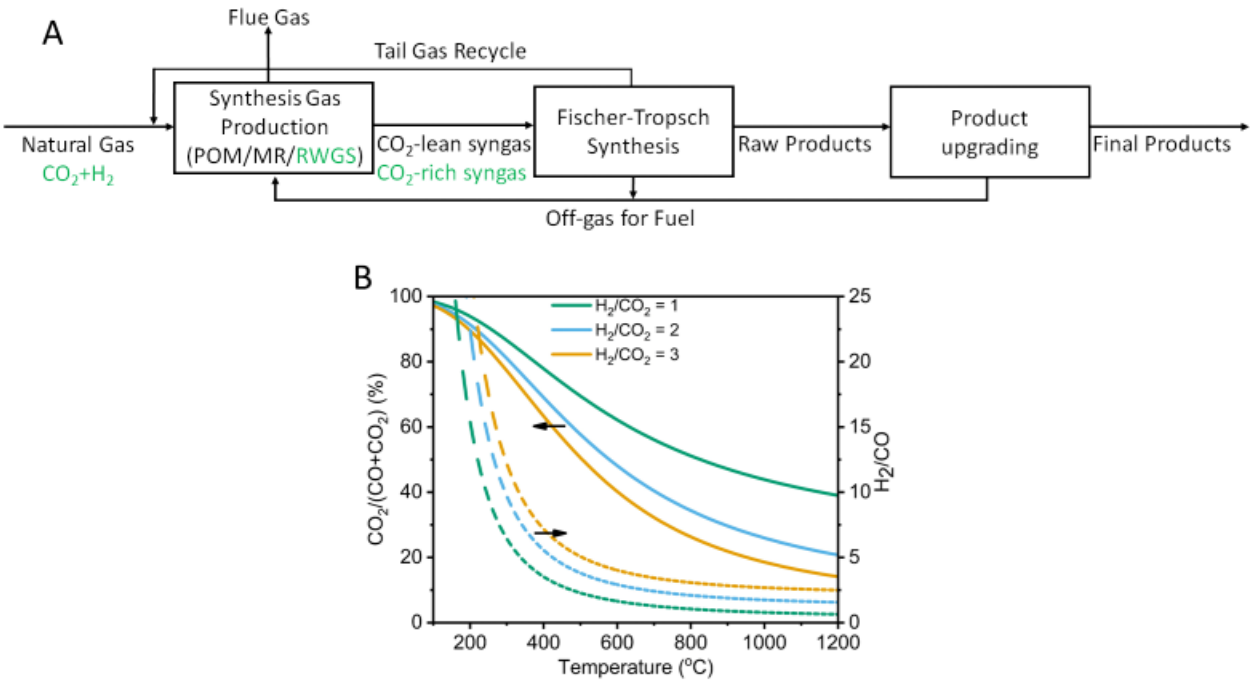

Figure 1. Process considerations for synthetic fuels production. a, A block scheme for gas to fuel production from methane (black) or a sustainable feed such as CO_2 emissions and renewable H_2 (green). Apart from the syngas production technology and composition, the processes are similar. **b,** Equilibrium composition in terms of CO_2 fraction (CO_2/(CO+CO_2)) and syngas ratio (H_2/CO) for the RWGS versus temperature at 21 bar.

2. Methods

Catalyst preparation. A Co/TiO_2 catalyst was prepared by incipient wetness impregnation as reported previously [45]. Cobalt nitrate hexahydrate (>99.0 %, <0.001 % Ni) and titanium dioxide nanopowder (>99.5 %, formally known as P25) from Merck were used. TiO_2 was pressed and sieved to a 75-150 μm fraction. To achieve a theoretical 6 % wt. Co loading, 0.32 g $Co(NO_3)_2*6H_2O$ was dissolved in 0.11 mL milliQ water and impregnated on 1 g of sieved TiO_2 (pore volume 0.23 $cm^3\ g^{-1}$). The impregnated TiO_2 was dried at 90 °C for 24 hours and subsequently pyrolyzed in a tubular oven under a flow of N_2 at 80 °C for two hours and followed by 250 °C for two hours with a ramping rate of 2 °C min^{-1}. The resulting material was sieved again to obtain a 75-150 μm catalyst.

Catalyst characterization. Different batches of Co/TiO_2 were used in this work, and the properties were checked to be consistent. To determine the elemental composition, X-ray fluorescence (XRF) analysis was performed with a Malvern PANalytical Epsilon3^{XLE} spectrometer. XRF determines the amount of Co_3O_4 based on fundamental parameters which is corrected to yield the cobalt loading. The metal loading was determined after calcination of the catalyst at 500 ºC to ensure all cobalt to be oxidized and precursor groups to be removed. The elemental composition was further examined using Inductively Coupled Plasma Optical Emission Spectrometry (ICP-OES) on a Perkin Elmer Optima 7000 DV. The transmission electron microscopy (TEM) images were made with a 200 kV Tecnai T20 electron microscope. The catalyst was dispersed in ethanol and placed on a carbon coated Cu grid. Elemental distribution was done in STEM mode on a SDD EDX detector (XmaxT80, Oxford instruments). X-ray diffraction (XRD) patterns were obtained on a Bruker Advance D8 diffractometer at 40 kV and 40 mA using Cu-Kα radiation (λ = 1.5544 Å). The 2θ angle was varied from 3° to 90° with a step size of 0.02 and a

scan time of 0.9 s. Nitrogen physisorption was measured with a Micromeretics ASAP 2420. The total surface area was determined by the Brunauer-Emmett-Teller (BET) method. Temperature Programmed Reduction/Desorption experiments (TPR/TPD) were executed on a Micromeretics AutoChem II 2920 equipped with a thermal conductivity detector (TCD). For the TPR experiments, a flow of 5 % H_2 in Ar was put over the catalyst (3000 mL g_{cat}^{-1} h^{-1}) and the temperature was ramped from 50-650 °C with a ramping of 1 °C min^{-1}. For CO and CO_2 TPD, the catalyst was reduced in situ at 350 °C for 8 hours with a ramping of 5 °C min^{-1} corresponding to the pretreatment isupportin the reactor. After this, the sample was cooled down to 50 °C under helium. The sample was put under a flow of 5 % CO in He for 1 hour for the CO TPD or 10 % CO_2 in He for the CO_2 TPD and ramped to 650 °C with 5-10 °C min^{-1}. The H_2-chemisorption was performed on a Micromeritics ChemiSorb HTP. The catalyst was reduced in situ (GHSV of 4800 and 24000 mL g_{cat}^{-1} h^{-1}) at 350 °C for 8 hours with a ramping of 5 °C min^{-1} after that the chemisorption was measured at a temperature of 150 °C with a ramping of 3 °C min^{-1}. The particle size is corrected for degree of reduction and based on hemispherical particles. TPR-MS was performed with an in-house developed reactor with a ramp of 5 °C min^{-1} while scanning for the masses 14-18, 28, 30, 32, 46, 62 and 63 u corresponding to the mass of hypothetical decomposition products.

Catalytic evaluation. The catalytic tests were performed in a stainless-steel reactor tube (inner diameter of 6 or 9 mm) in a MICROACTIVITY-Effi from PIDEngTech. Ar (99.999 %), H_2 (99.999 %), CO_2 (99.999 %) and CO (99 %) were fed to the setup by mass flow controllers from Bronkhorst. The catalyst mass was diluted 5 times with silicon carbide (50-75 μm) to ensure isothermal operation [55]. Plug flow was ensured by keeping the diameter of the particles at least 10 times smaller than the diameter of the reactor and the length of the bed was at least 50 times the

diameter of the particle [55]. The Weisz-Prater criterion, given in Supporting Information, was used to confirm the absence of internal mass transfer limitations.

Reduction of the catalyst (0.1-1.0 g) was performed under a flow of 20 mL min^{-1} of 25 % v. H_2 in Ar at 350 °C at 2 bar with a heating ramp of 1 °C min^{-1} for 8 hours. After reduction, the reactor was cooled to 220 °C (1 °C min^{-1}) and the pressure was increased to 21 bar (5 bar min^{-1}) for the FTS experiments. During the reaction, the flows of Ar, H_2, CO and CO_2 were varied. To enable a good comparison, the ratio H_2/CO_x was kept at 2/1, and the flow of Ar was equal to the flow of $CO+CO_2$. This means that for any GHSV, the $CO+CO_2$ content was 25 % v., the Ar content was 25 % v. and the H_2 content was 50 % v. The only exception is the experiments where CO_2 was replaced with Ar. All catalyst evaluation data were collected at steady state for at least 4 hours per reaction condition. A representative run program is included Figure S1. The program steps were generally repeated in reverse to check for stability and reproducibility as depicted in Figure S2. The reactor unit was equipped with an online gas chromatographer for the analysis of the product stream. A Thermo TraceGC 1310, equipped with a ShinCarbon ST and Hayesep Q column and a thermal conductivity detector was used for the analysis of the permanent gases and a GS-gaspro and Stabilwax column both equipped with flame ionization detector were used for the C_1-C_{10} fraction The chain growth probability was determined from the C_3-C_8 product fraction as heavier hydrocarbons partly start to be condensed out in the cold trap (70 °C, 1 bar).

The conversion of CO and CO_2 were determined by equation 1 and 2 respectively. The C_{5+}-selectivity was calculated using equation 3. The produced gasses were corrected for volume changes by the internal standard Ar. The value for chain growth probability constant (α), governed by the Anderson-Schulz-Flory distribution model, was obtained by determining the slope of $Ln(W_n/n)$ versus n for C_3-C_8 and calculating the exponential (equation 4).

$$X_{CO} = \frac{[CO]_{in} - \frac{[Ar]_{in}}{[Ar]_{out}} * [CO]_{out}}{[CO]_{in}} \quad (1)$$

$$X_{CO_2} = \frac{[CO_2]_{in} - \frac{[Ar]_{in}}{[Ar]_{out}} * [CO_2]_{out}}{[CO_2]_{in}} \quad (2)$$

$$[C_{5+}](\%) = 100\ \% - \frac{\frac{[Ar]_{in}}{[Ar]_{out}}[C_{1-4}]}{[CO]_{in} - \frac{[Ar]_{in}}{[Ar]_{out}} * [CO]_{out} + [CO_2]_{in} - \frac{[Ar]_{in}}{[Ar]_{out}} * [CO_2]_{out}} \quad (3)$$

$$\frac{W_n}{n} = (1-\alpha)^2 \alpha^{n-1} \quad (4)$$

Isotopic labeling $^{13}CO_2$ experiments at steady state. A 99.0 atom % ^{13}C labelled CO_2 gas cylinder of 0.42 L from Merck was pressurized with unlabeled CO_2 (99.999 %) to 25 bar. The mixture of labeled CO_2 was mounted to the Effi-setup and the setup gas lines were flushed. A catalytic evaluation was performed at 220 °C and 2 bar with pretreatment as described above. The experiments were conducted with a feed with a CO_2 fraction of 50 % and 90 % at 220 °C with a GHSV from 300 to 3400 mL g_{cat}^{-1} h^{-1}. To obtain data on full CO conversion, the temperature was increased to 260 °C. To detect and quantify the isotopic species, Tedlar gas bags were filled with the gas mixture and evaluated on an Agilent 6890 GC-MS equipped with a GASPRO column using a gas tight syringe. The $^{13}CH_4$ and $^{12}CH_4$ counts were determined from the ^{17}counts and ^{16}counts from which the water contribution was subtracted based on the water ratio from NIST database.

In-situ diffuse reflectance infrared Fourier transform spectroscopy. *In-situ* diffuse reflectance infrared Fourier transform spectroscopy (DRIFTS) was employed to study formation of intermediates during the reaction. The reaction was carried out using a Nicolet iS10 FTIR spectrometer with a MCT detector and a custom-made Harrick Low Dead Volume High Temperature Reaction Chamber DRIFTS reactor and temperature controller (Figure S3). Spectra

were recorded in series roughly every 22 s. The sample was first reduced *in-situ* in the DRIFTS cell while heating from room temperature to 350 °C at 1 °C/min with a flow of 5 ml/min H_2 and 15 ml/min Ar. Once 350 °C was reached, the temperature was held under the same flow for another 2 h. Subsequently, the sample temperature was decreased to 220 °C with a 1 °C/min ramp rate in 20 ml/min Ar. The gas flow was then changed to 90/10 Low (per the flows listed in Table 1), and the pressure was ramped to 3 bar using a Bronkhorst EL-PRESS back pressure regulator. The experiments commenced after a stable pressure of 3 bar was reached. After ~1 h, the gas composition was switched to 90/10 Full. Another ~1 hour was maintained at this condition before switching to the following condition. Each condition was maintained for at least 60 min while recording spectra. In the latter part of the experiment, the reaction conditions were repeated in reverse to assess whether the sequence had an impact on the observed mechanism. The full spectra are depicted in Figure S4.

Table 1. Flow rates (ml min^{-1}) of different reaction conditions.

	H_2	Ar	CO	CO_2	CO inlet (%)	H_2/CO
90/10 Low	30.25	15.13	1.51	13.61	2.5	20
90/10 Full	13.75	6.88	0.69	6.19	2.5	20
50/50 Low	11.92	5.96	2.98	2.98	12.5	4
50/50 Full	1.83	0.92	0.46	0.46	12.5	4

Thermodynamic calculations. All thermodynamic calculations were performed with Aspen Plus. For the RWGS equilibrium, an equilibrium reactor was modelled, and the compositions were calculated with the Peng-Robinson equations of state. A sensitivity analysis was performed to plot the effect of temperature, pressure and feed ratios on the product distribution of the RWGS. As methane formation in the RWGS should be suppressed in the syngas production, methanation was

not included in the thermodynamic calculations and hence there was no effect of pressure on the equilibrium composition.

Kinetic modeling. For determining the kinetic constant of the Fischer Tropsch reaction, MATLAB was used to fit two data sets in one routine. The rate orders were used as obtained in the work of Zennaro as -0.24 and 0.74 for α and β respectively [52]. The fitting was carried out using the lsqnonlin routine, where the mass balance (equation 5) including the change in density (equation 6) was solved using the built-in ode45 MATLAB function. For ϵ a value of -0.25 is taken which corresponds to the change in gas density for the production of butene. Subsequently the resulting kinetic constant, combined with the rate orders were taken as input to plot the integral conversion as a function of catalyst weight and the CO molar feed rate, taking into account the feed ratios as employed for the individual experiment. In addition, an error landscape was constructed by varying the input of α and β to gain insights in fit quality and provide other options for α and β in this dataset.

$$\frac{dF_{CO}}{dW} = R_{CO}{}' = -k_1 C_{CO}^{\alpha} C_{H2}^{\beta} \qquad (5)$$

$$\phi_v = \phi_{v0} * (1 + \epsilon X_{CO}) \qquad (6)$$

DFT calculations and microkinetic model. Periodic spin−polarized DFT calculations were conducted using the vdW−DF functional, a plane−wave basis set with a cut−off kinetic energy of 450 eV, and the projector−augmented wave method as implemented in the Vienna Ab−initio Simulation Package (VASP) [56–60]. The construction of the cobalt terrace sites and B5 step sites are described in an earlier publication, including the microkinetic model construction [53]. Microkinetic simulations, using a mean-field approach, were performed using the Chemkin® software [61]. An isothermal 1D plug flow reactor model was used in the simulations to calculate reaction rates, surface coverages and concentration profiles along the reactor. We used a CO_x inlet flowrate of

290 $mmol_{COx}$ h^{-1} and an active site density of 300 $mmol_{active\ sites}$ kg_{cat}^{-1}. The equations were solved up to the specified conversion (X_{CO} = 10 %), to stay in low-conversion kinetic limit, by varying the amount of catalyst. Chemkin® solves the ordinary microkinetic differential equations using a modified DASPK solver with a relative tolerance of 10^{-6} and an absolute tolerance of 10^{-9} to obtain convergence[62] . An example of the input files for the high coverage simulations is provided in the Zenodo repository [63]. For the initial coverage, θ_* and $\theta_\#$ were set to 1. Selectivities and average TOFs were calculated after 10 % conversion using molar outlet flow rates. Surface coverages are reported at 10 % conversion.

CO_2-FT microkinetic model. For the microkinetic simulations at CO saturation coverage, the model developed in the Saeys group was used, which is publicly available in the Zenodo repository and described in a prior publication [53,63]. Some minor adjustments were made to the model to accommodate CO_2 hydrogenation (Table S1). The experimental reaction energy of the reverse water-gas shift is 28.5 kJ/mol [64]. The DFT vdW-DF value is 55.1 kJ/mol. Therefore, the CO_2 gas phase energy was corrected by +26.6 kJ/mol, as has become standard in microkinetic DFT simulations [65–68]. In the original FT model, H_2 only adsorbs non-competitively with CO* (H_CO*), i.e., it adsorbs in a unit cell containing 7 CO*'s. This was implemented because CO* adsorption is significantly more exergonic than H* adsorption at FT conditions. When the CO partial pressure decreases and the H_2/CO ratio increases, H_2 adsorption however becomes competitive with CO adsorption. Therefore, an additional H* intermediate was added that adsorbs competitively with CO* (H*) in a unit cell with 6 CO*'s. This was implemented by including fast diffusion of H* surrounded by 7 CO*'s (non-competitive H*) to a unit cell with only 6 CO*'s (competitive H*). Lastly, CO_2 activation on the CO- and C-saturated B5 site was not described in the original model. Using a BEP relation with α=0.5 the activation energy for $CO_2^\# + * \rightarrow CO^\# + O^*$ was determined.

Since CO_2 adsorption on the CO- and C-saturated B_5 site is strongly endothermic (92 kJ/mol), the reaction was modelled as a dissociative adsorption. The high activation barrier (128 kJ/mol) and strong endothermicity of CO_2 adsorption suggest that this route is not viable, no matter the exact energy of the transition state, making the BEP estimate activation energy a sufficient approximation.

3. Results and discussion

Catalyst. Co/TiO_2 is a relevant FTS catalyst and has been extensively investigated [36–43]. A Co/TiO_2 catalyst was prepared by incipient wetness impregnation and characterized using XRF, ICP, TEM, XRD, N_2-physisorption, H_2-chemisorption and TPD/TPR. Table 2 provides a summary of relevant catalyst properties. The cobalt elemental loadings determined by XRF and ICP were similar at ~5 % wt. (Table 2). XRD and TEM (Figure S5 and S6) of the fresh catalyst suggest a homogenous dispersion of cobalt as no large cobalt oxide nanoparticles were observed [36,37,39,40,44,45]. Chemisorption (Table 2) of the reduced catalyst and STEM-EDX (Figure S6) of the spent catalyst identified cobalt nanoparticles with an average particle size of 30 nm. This suggests the stability of cobalt nanoparticles during reaction and, importantly, demonstrates that the catalyst is independent of the 'particle size effect' which is prominent for cobalt nanoparticles less than 6 nm [5,46]. TPR (Figure S7) showed peak maxima of CoO reduction at 350 and 380 °C, respectively, for 1 and 5 °C/min heating rate. H_2-chemisorption showed a degree of reduction of 90 % after 150 minutes at 350°C. This required reduction temperature agrees with literature [36,37,43–45, 47]. Thus, to ascertain cobalt reduction before catalytic experiments, reduction was performed at 350 °C and extended for 8 hours.

Table 2. Catalyst properties determined using XRF, ICP, H_2 chemisorption and N_2 physisorption.

	Co/TiO_2
Cobalt wt. loading (from ICP, %)	4.8 ± 0.5
Cobalt wt. loading (from XRF, %)	4.9 ± 0.1
Chemisorption average particle size (hemisphere) (nm)	31 ± 3
Chemisorption degree of reduction (%)	90 ± 2
BET surface area ($m^2\ g^{-1}$)	52 ± 3
BJH pore size (nm)	30 ± 3

CO_2-containing synthesis gas. The catalytic performance for hydrogenation of CO, CO_2 and mixed-feeds is shown in Figure 2a while the stability and the complete product spectrum are shown in Figure S8. With a feed of H_2/CO_2 = 2/1 (CO_2 FTS), 96 % methane selectivity and no CO and C_{5+} hydrocarbons were observed at 6 % CO_2 conversion. With a feed of H_2/CO=2/1 (CO FTS), 83 % C_{5+}-selectivity was achieved at 10 % CO conversion. The mixed CO/CO_2 FTS feed (H_2/CO_2/CO = 4/1/1) showed a C_{5+}-selectivity of 80 % at 31 % CO conversion but no CO_2 conversion was observed. In comparison to CO FTS, the increase in CO conversion with the mixed-feed is attributed to both higher CO residence time and H_2/CO = 4. The 3 % decrease in C_{5+}-selectivity corresponded to a 3 % increase in methane selectivity (Figure S8) and a slightly lower chain growth probability, α (Figure S9). These differences in product selectivity could be due to CO conversion, H_2/CO ratio, CO methanation and/and CO_2 methanation, i.e. the Sabatier reaction and in the following, we will discriminate between these different explanations. Notably, this is the highest C_{5+}-selectivity reported for mixed CO/CO_2 FTS feeds with a CO_2 fraction up to 50 % [23–34].

Figure 2b shows the hydrocarbon selectivity versus conversion for a feed with 50 % CO_2 fraction. The hydrocarbon selectivity remained stable between 20 and 80 % CO conversion. An identical α of 0.86 was attained (Figure S10). No CO_2 conversion was observed. This rules out CO conversion as the origin of the higher methane selectivity in CO/CO_2-FTS compared to CO FTS.

To investigate the influence of CO_2 fraction in mixed-feed FTS on product selectivity, the CO_2 fraction was varied from 0 to 100 %, while the H_2/CO_x ratio and CO conversion were kept at 2 and 10 to 30 %, respectively (Figure 2c). C_{5+}-selectivity remained stable between 78 and 85 % when the CO_2 concentration was varied between 0 up to even 75 %. A decrease in liquid selectivity occurred only at CO_2 fractions of 90 and 100 %, and was mostly the result of increased methane selectivity from 23 to 96 % with only a small contribution (< 5 %) of the C_2-C_4 fraction. From Figure 2d, this decrease in C_{5+}-selectivity appears to correlate with the decreasing outlet partial pressure of CO, and an increase in H_2/CO ratio.

Thus far we demonstrated that the co-feeding of CO_2 with syngas was possible with high C_{5+}-selectivity of 78 to 85 % within the set boundaries of feed with a CO_2 fraction below 75 % at 10 to 30 % CO conversion (referred as Case 1: FTS). C_{5+}-selectivity decreased from 78 to 54 % when the fed CO_2 fraction increased from 75 to 90 %. Interestingly, α remained between 0.82 and 0.85 (Figure S11), suggesting negligible change in chain growth probability. Instead, this decrease in C_{5+}-selectivity corresponded to an increase in methane selectivity, which is formed from CO or/and CO_2. From Figure S12, an increase in H_2/CO outlet ratio for a feed with 50 % CO_2 fraction corresponded to a decrease in C_{5+}-selectivity and an increase in methane selectivity. α stayed stable at 0.84 ± 0.01 (Figure S13). Hence, when the H_2/CO outlet ratio is significantly higher than 10, the increase in methane selectivity is attributed to CO methanation (referred as Case 2: CO methanation). CO and CO_2 are proposed to adsorb on the same Co sites, with CO adsorption being

more favorable, we postulate that sufficient CO prevents CO_2 adsorption and reaction [30]. Hence, CO_2 methanation occurs only when CO partial pressure is low. For a feed with 90 % CO_2 fraction, methane selectivity increased when CO conversion was above 70 % (Figure S14). At 93% conversion, chain growth probability dropped to 0.73 (Figure S15), indicating CO_2 methanation (referred as Case 3: CO_2 methanation). At 70 % CO conversion, about 0.2 bar (0.75 v%) of CO is present in the outlet. This indicates that a partial pressure of CO of 0.2 bar should be present to avoid Case 3: CO_2 methanation. The CO partial pressure in the effluent stream depends both on CO partial pressure in the inlet, and on CO conversion. Hence, a plot of C_{5+}-selectivity and the effluent partial pressure of CO in the experiments with different CO levels is included in Figure S16.

For efficient mixed-feed FTS, methane production must be minimized, so Case 1 operation is ideal. Figure 2e illustrates the three cases, where CO conversion is varied for the fed CO_2 fraction of 50 %. The H_2/CO outlet ratio remained below 10 for all conversions except at 80 %. The CO outlet partial pressure remained above 0.2 bar for all conversions. Therefore, the system operates in the FTS regime (Case 1) until 80 % CO conversion, where CO methanation (Case 2) becomes a risk. Figure 2f illustrates the three cases, where CO conversion is varied for the fed CO_2 fraction of 90 %. The H_2/CO outlet ratio is above 10 throughout the conversion range, so the system is always operated with increased CO methanation (Case 2). This explains the higher methane selectivity compared to the 50 % CO_2 fraction in Figure 2e. Above 90 % CO conversion, the CO outlet pressure drops below 0.2 bar, shifting the system to Case 3 where CO_2 methanation likely occurs. This explains the increase in methane selectivity from CO conversion of 90 % onwards to ultimately 80 %, which indicates that aside from CO methanation, CO_2 methanation is likely taking place. The boundary process conditions for Case 1, 2 and 3 are given in Table 3.

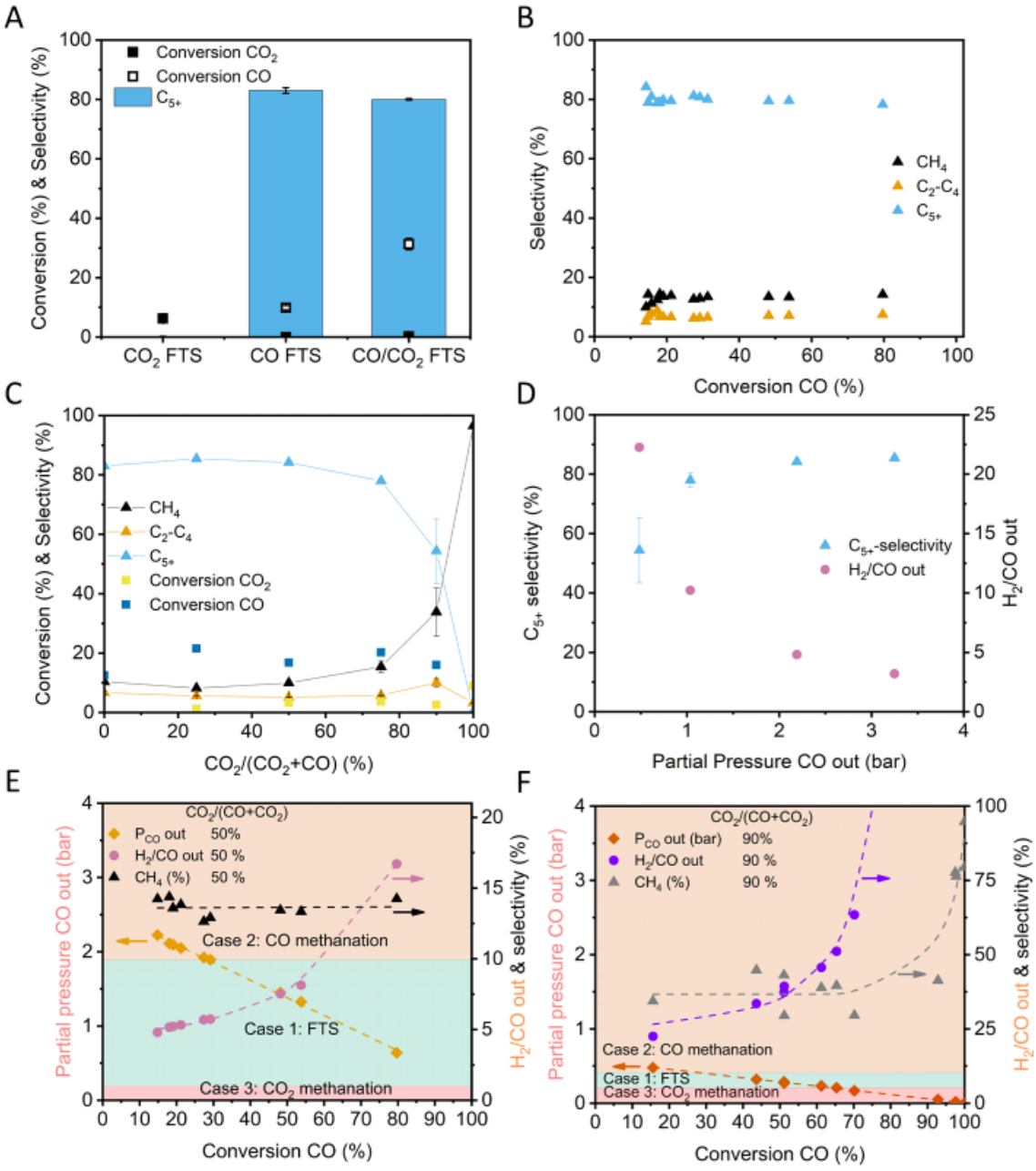

Figure 2. CO_2 co-feeding with synthesis gas over Co/TiO_2 at 220 °C and 21 bar. **a,** CO_2 FTS with $H_2/Ar/CO_2$=2/1/1, CO FTS with $H_2/Ar/CO$=2/1/1 and mixed CO/CO_2 FTS with $H_2/Ar/CO_2/CO$=4/2/1/1 at ~4000 mL g_{cat} h^{-1}. **b,** Selectivity as a function of CO conversion (by GHSV variation) for a feed with CO_2 fraction of 50 % ($H_2/Ar/CO_2/CO$=4/2/1/1,). **c,** Effect of CO_2 fraction in mixed-feed FTS at H_2/CO_x=2 and 10 to 30 % CO conversion. **d,** Relationship between partial pressure and H_2/CO feed ratio on C_{5+}-selectivity at 10 to 30 % CO conversion. **e,** Effect of

conversion on outlet CO partial pressure, outlet H_2/CO ratio and methane selectivity for the feed with a 50 % CO_2 fraction. Regimes 1,2 and 3 (FTS, CO methanation and CO_2 methanation) are visualized in green, orange and red. Dashed lines are added to clarify trends. **f,** Effect of conversion on outlet CO partial pressure, outlet H_2/CO ratio and methane selectivity for the feed with a 90 % CO_2 fraction. Regimes 1,2 and 3 (FTS, CO methanation and CO_2 methanation) are visualized in green, orange and red. Dashed lines are added to clarify trends.

This finding that the main contributor to lower C_{5+} selectivity in mixed-feed FTS originates from extra production of methane, is in line with earlier reports [25,27,28]. However, the important new insight is that in our results the drop in selectivity is not seen until reaching 90 % CO_2 fraction, whereas in the cited literature this was already reported for feeds above 40 %. The key difference is that earlier investigations worked at complete CO conversion, which caused a significant gradient in CO partial pressure over the packed bed reactor, with complete absence of CO towards the end of the reactor. This means that CO_2 methanation as described in Case 3 occurred. To avoid this pitfall, CO conversion should be limited which is achieved by varying GHSV.

Table 3. Boundary conditions which determines role of CO2 in mixed CO/CO_2 FTS feeds, and the origin of higher methane production for the system at 220 °C and 21 bar.

Regime	Effluent CO partial pressure (bar)	Effluent H_2/CO ratio	CO_2 function	Origin of higher methane production
1. FTS	Greater than 0.2	Below 10	Inert	Normal FTS
2. Risk of CO methanation	-	Above 10	Inert	CO methanation
3. CO_2 methanation	Less than 0.2	-	Reactive	CO_2 methanation

Reactivity of CO_2. To demonstrate CO_2 acts as an inert when the CO partial pressure exceeds 0.2 bar, CO_2 was replaced with Ar in the mixed-feeds (Figure 3a). With identical inlet partial pressure and H_2/CO ratio, both feeds indeed gave similar CO conversion and C_{5+}-selectivity, confirming the inertness of CO_2 as described in Case 1 and 2. The complete product distribution is included in Figure S17. The lower C_{5+}-selectivity for experiments with increased CO_2 fractions is thus caused by a higher H_2/CO ratio, and not CO_2 methanation.

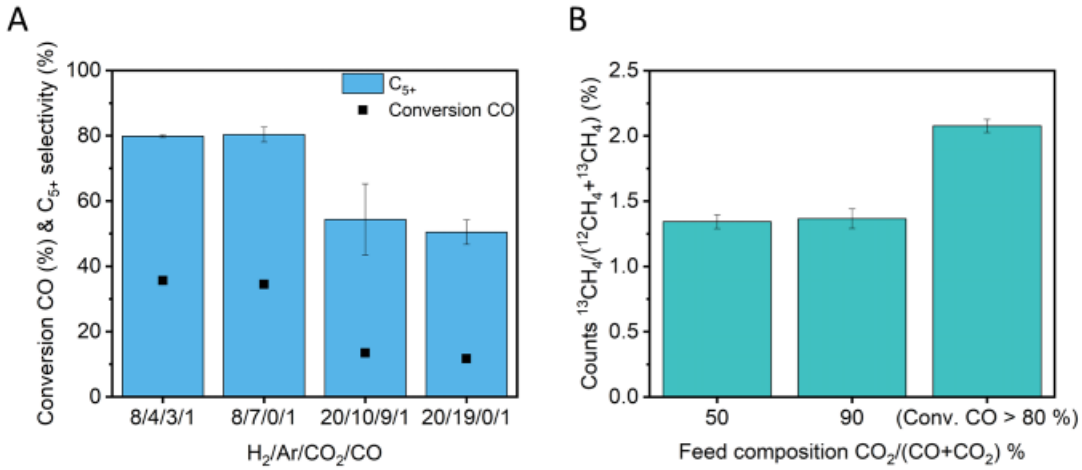

Figure 3. Verification of CO_2 reactivity. a, CO conversion and C_{5+} selectivity of two sets of feeds with same CO concentration upon CO_2 replacement with Ar at 220 °C, 21 bar with a GHSV of 4900-85000 mL g_{cat}^{-1} h^{-1}. **b,** Using $^{13}CO_2$ in mixed-feed FTS at 220 to 260 °C, 2 bar with a GHSV of 344 to 3444 mL g_{cat}^{-1} h^{-1} to demonstrate no CO_2 contribution in the formation of methane under CO conversion below 80 %. The conversion and selectivity are included in Table S2.

Additionally, $^{13}CO_2$ labelling experiments were performed to verify our hypotheses for the various cases. The catalyst was tested with a mixture of $^{13}CO_2$ in mixed-feeds at 220 °C and 2 bar (Figure 3b), with conversions and product distribution in Table S2. When CO_2 is inert, no $^{13}CH_4$ besides the natural isotope occurrence would be formed from $^{13}CO_2$ mixed-feeds. For both feeds

with 50 % and 90 % CO_2 fractions, no additional $^{13}CH_4$ were observed when CO conversion was below 40 %. This confirms the inert nature of CO_2 in Case 2 and points to CO methanation as the cause for the increased methane levels when 90 % CO_2 fraction was fed. By increasing the temperature to 260 °C, CO conversion increased to 80 % and the increase in $^{13}CH_4$ confirmed that $^{13}CO_2$ methanation occurred in the absence of sufficient CO as in Case 3.

In-situ DRIFTS. To probe CO surface coverages in mixed-feed FTS, *in-situ* DRIFTS experiments were performed. DRIFTS spectra were recorded at 3 bar and 220 °C while the feedstock was switched with adjustment of the GHSV between "Low" and "High" for a CO_2 fraction of 90 % and 50 %). Further details are included in the Methods section. Figure 4a depicts one representative DRIFTS spectrum at each reaction condition for the CO absorption region (2250-1700 cm^{-1}). Several peaks can be observed at the different conditions, including adsorbed CO (denoted as *) at 2037 cm^{-1} and 2012 cm^{-1}, which are both ascribed to linearly adsorbed CO [48,49]. Further adsorbed species were observed in Figure S18. Figure 4b shows the intensities of these peak positions, normalized to the trough of $CO_{(g)}$ – i.e., its IR-forbidden Q-branch (2143 cm^{-1}), ascribed to adsorbed CO over the course of the experiment. It is important to note that these intensities should be interpreted qualitatively, where within a given feed composition (i.e., 90 % CO_2 fraction or 50 % CO_2 fraction, whether low or high GHSV) time-resolved trends allow us to correlate species and their behavior.

A clear difference between a CO_2 fraction of 90 % and 50 %, is the predominance of the wavelength at which CO* is observed. For a 50 % CO_2 fraction, the peak at 2037 cm^{-1} dominates, while for 90 % CO_2 fraction, CO* appears at 2012 cm^{-1}. Upon the change from 90 % CO_2 fraction to 50 % CO_2 fraction, the observed time-dependent decrease of 2012 cm^{-1} is anticorrelated to the increase in 2037 cm^{-1}, indicating a shift of CO* to higher wavenumbers which is likely due to

higher coverage of CO* on the cobalt surface [50,51]. The increase in normalized intensity of CO* species with increased CO partial pressure, i.e., comparing the feed composition of 90 % CO_2 fraction to 50 % CO_2 fraction further validates a higher coverage of CO* at higher CO partial pressures.

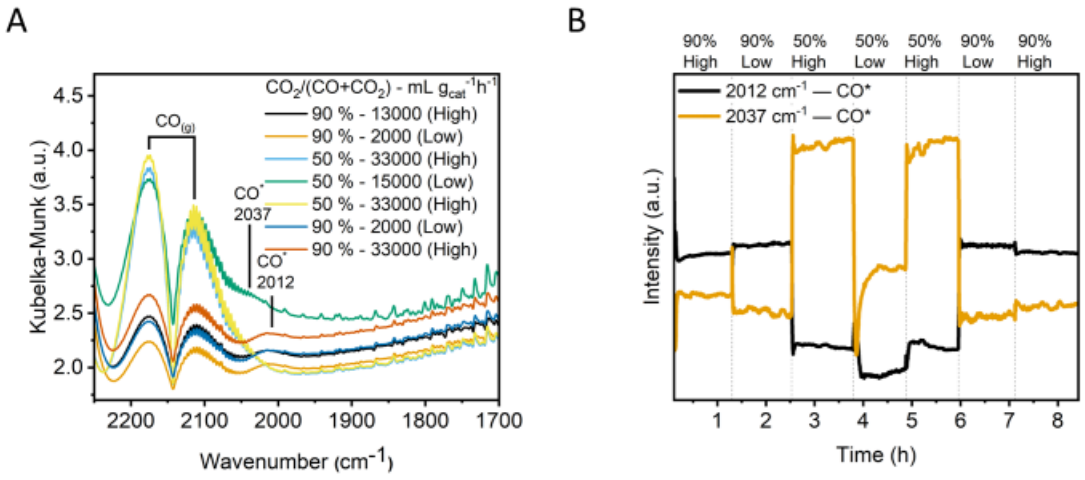

Figure 4. In-situ DRIFTS conducted under Low and High GHSV at 3 bar and 220 °C. a, One representative spectrum is shown for each gas composition. Intermediate species are labeled in the graphs. **b,** Intensity vs time-on-stream of adsorbed CO at 2012, and 2037 cm^{-1}. Intensities are normalized to the trough of $CO_{(g)}$, 2143 cm^{-1} to account for the effect of changing concentration of reactants $CO_{(g)}$ and $CO_{2(g)}$ absorbing in the same region.

Kinetic modeling. As described above, numerous experimental approaches were employed to identify the descriptors and boundary conditions in which CO_2 co-feeding resulted in a higher methane selectivity. A minimum CO outlet partial pressure of 0.2 bar is required to achieve sufficient CO surface coverage, essential for suppressing CO_2 methanation. When this condition is met, the kinetics of mixed CO/CO_2 feed FTS resemble conventional CO FTS. Hence the data for the 50 % CO_2 fraction is fitted to a power law kinetic model where $R_{CO}{}' = -k_1 C_{CO}^{\alpha} C_{H2}^{\beta}$. With a negative reaction order for CO, α (0 to -1), the reaction order for H_2, β, should be at least 0.5 to

obtain a reliable fit (Figure S19). Zennaro et al investigated the kinetics of a Co/TiO_2 catalyst in a packed bed reactor and reported α and β values of -0.24 and 0.74 respectively [52]. Using these values to fit our experimental data (Figure 5), the kinetic constant was determined to be 65.8 $mol^{0.5}L^{-0.5}\ s^{-1}$. The good fit supports the reliability of the results and is further evidence for the inert nature of CO_2 in Case 1 and 2.

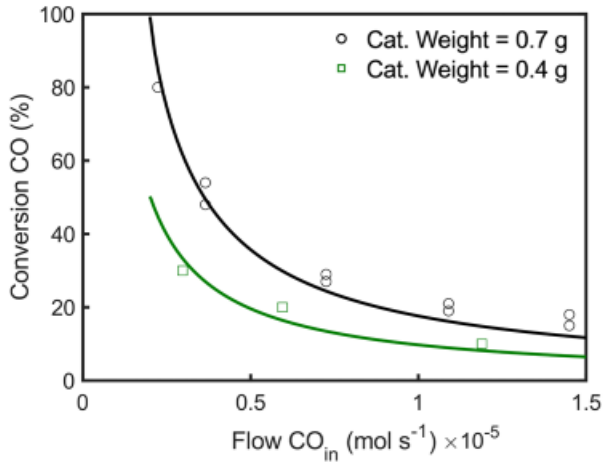

Figure 5. Fitting of kinetic data for a feed with a 50 % CO_2 fraction at 220 °C, 21 bar with reaction orders (α and β) of -0.24 and 0.74 respectively.

Microkinetic modeling. To evaluate the effect of the CO_2 fraction in the feed, mixed-feed hydrogenation was simulated using the recently developed first principles dual-site microkinetic model for CO hydrogenation [53]. This model includes over 600 elemantary reactions up to C_{16} hydrocarbons, and explicitly includes a high CO coverage of between 0.5 and 0.6 monolayer (ML) [51,54]. Moreover, the CO- and C-saturated B_5 site (dual site) are modelled to represent step sites, with surface diffusion included. To describe reactions at lower CO partial pressures, competitive H^* adsorption was included in addition to the non-competitive adsorption in the original model [53]. To account for CO_2 activation, an additional CO_2 activation pathway at B5 step sites was included, and the gas phase energies for the RWGS from DFT were corrected by changing the gas phase

energy of CO_2 to accurately reflect thermodynamic equilibrium. This correction is important to describe CO_2 methanation, where the RWGS is often quasi-equilibrated, but had a limited effect on the CO_x hydrogenation kinetics under FT conditions [53]. Further details are included in the Methods section.

Similar to the described experiments, the CO_2/CO feed ratio was increased while keeping the CO conversion constant at 10 % (Figure 6a). The model predicts a very slight decrease in C_{2+} selectivity (80.5 % to 80.1 %) and corresponding increase in CH_4 selectivity (17.9 % to 18.6 %) when CO is replaced by CO_2 in line with the limited changes observed from experimental results. The chain growth probability decreases slightly from 0.775 to 0.766 when the CO_2 fraction is increased to 50%, and to 0.733 at a CO_2 fraction of 80 %. CO_2 activation is very slow under these conditions (10^8 times slower than CO activation), and CO_2 formation on the terrace site $CO^* + O^* \rightarrow CO_2^* + *$ is slightly faster than CO_2 consumption. The slow CO_2 activation is rationalized from the Gibbs free energy profile at CO saturation coverages (Figure 6b, dotted lines). All four CO_2 activation pathways depicted in Figure 6b at saturation CO coverage have free energy barriers over 150 kJ/mol. At low CO coverage, several of these free energy barriers are below 100 kJ/mol, and it follows that the prevalence of CO_2 activation is very sensitive to the CO coverage. Alternative CO_2 activation pathways, e.g., via HCOO*, were calculated, but did not contribute significantly to CO_2 activation (Figure S20).

Increasing the CO_2 fraction in the feed to 80 % and reducing the CO inlet partial pressure below 1 bar begins to impact the CO coverage due to competitive hydrogen adsorption. At this CO_2 fraction, the CO coverage reduces to 0.527 ML, close to the limit of the saturation coverage of the microkinetic model, 0.5 ML. A separate low CO coverage, dual-site CO_2 methanation model was used to simulate the experiments with a high CO_2 inlet fraction [53]. In this model, CO_2 is readily

activated to adsorbed CO*, consistent with the low activation energies in Figure 6b, which undergoes further hydrogenation to methane. The CO* coverage in these models is between 0.25-0.35 ML and methane selectivities over 95 % are predicted for a CO_2 conversion of 10 %.

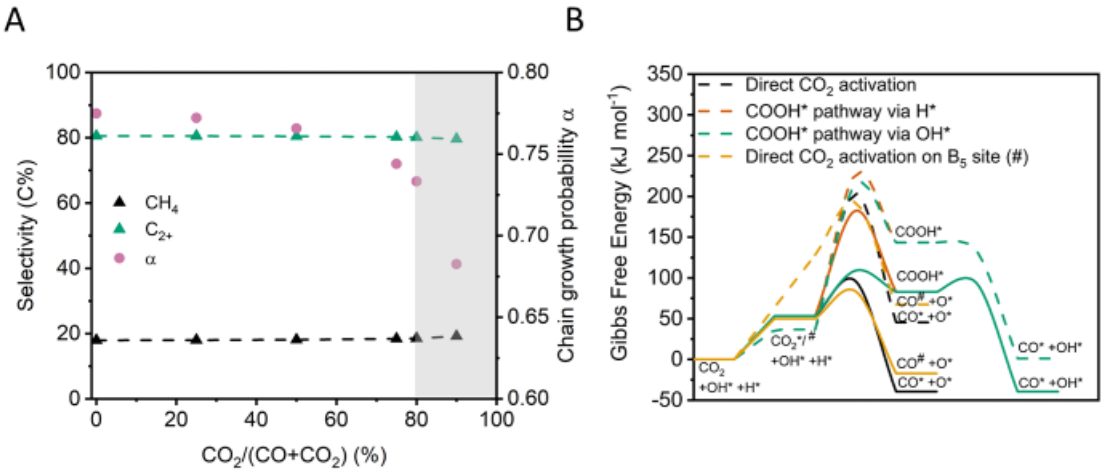

Figure 6. Microkinetic modeling to simulate the effect of CO_2 co-feeding with synthesis gas. **a,** Selectivity for CH_4 and C_{2+}, and chain growth probability for simulations with an increasing CO_2 fraction (500 K, 20 bar, H_2:CO_x:Ar ratio of 2:1:1, X_{CO} = 10 %), using kinetic and thermodynamic parameters calculated on CO−saturated cobalt terraces and on carbon and CO−saturated B5 step sites [53]. The grey area indicates the region where the Fischer-Tropsch microkinetic model is not valid anymore and low CO coverage kinetics become relevant. **b,** Free energy diagram for CO_2 activation pathways on the terrace site, including OH* assisted pathways, and CO_2 activation on the B_5 site. Full lines represent the low CO coverage (0/9 ML CO) DFT calculations and dashed lines the saturation CO coverage (6/12 ML CO) DFT calculations. Terrace sites are indicated by * and B_5 sites are indicated by #. Balancing OH_x* (x=0,1,2) groups are left out for clarity.

The relatively stable hydrocarbon distribution and chain growth probability for CO_2 fractions up to 80 % agree with experimental results. In addition to the experimentally identified descriptors of

H_2/CO ratio, CO partial pressures and coverages, the microkinetic model identified that a high CO coverage suppresses CO_2 activation and competitive H_2 adsorption could increase methane selectivity in a high CO_2 co-feeding environment.

4. Conclusion

The possible involvement of CO_2 in mixed-feed FTS was investigated using an industrially Co/TiO_2 catalyst. The identified process boundary conditions for limited methane production are governed by CO partial pressure and H_2/CO ratio. At 220 °C and 21 bar, the boundaries are a CO partial pressure above 0.2 bar and a H_2/CO ratio of below 10/1. CO_2 was unreactive up to 90 % CO_2 fraction at CO conversion below 70 %. The inertness of CO_2 was first verified by replacement of CO_2 with another inert gas (Ar) and subsequently by $^{13}CO_2$ isotopic labeling. Operando DRIFTS correlated the gas composition with CO surface coverage. The good fit of the mixed-feed FTS data to a power law kinetic model of conventional FTS supports the notion that CO_2 is inert under the above conditions. Mixed-feed hydrogenation was simulated using a first principles dual-site microkinetic model for CO hydrogenation, including competitive H_2 adsorption and CO_2 activation. Microkinetic modelling revealed that CO_2 activation is slow when there is sufficient CO coverage, as in Case 1, which preserves the C_{2+} selectivity. In contrast, insufficient CO coverage, as occurs in Case 2 and 3, readily allows CO and CO_2 methanation. The CO and H_2 coverages are crucial descriptors that determine the hydrocarbon distribution and accordingly, CO partial pressure and H_2/CO ratio are key process parameters for efficient mixed-feed FTS.

ASSOCIATED CONTENT

Supporting Information. Supporting Information includes supporting methods, catalyst characterization, catalytic results for CO_2-containing synthesis gas, reactivity of CO_2, *in-situ* DRIFTS, kinetic modeling and microkinetic modeling.

AUTHOR INFORMATION

Corresponding Author

* jingxiu.xie@rug.nl

Author Contributions

B.C.A.d.J. synthesized, characterized, performed and conceptualized catalytic tests and drafted manuscript. K.T.R. built and analyzed the microkinetic theoretical model. T.R. performed and analyzed *in-situ* DRIFTS P.v.d.T. performed kinetic modeling. L.R. contributed to the design and data analysis of the isotopic labelling experiments. G.L.B. contributed to conceptualization of experiments, data analysis and discussion. H.J.H. contributed to data analysis and discussion. M.S. built and analyzed the microkinetic theoretical model and contributed to discussions. C.V. analyzed *in-situ* DRIFTS and contributed to discussions. J.X. conceptualized the project and experiments, conceived and supervised the entire study, and provided resources All authors reviewed and contributed to the final manuscript.

Notes

DATA AVAILABLILITY

The data presented in the figures of this paper will be publicly available via Zenodo. Other supporting data are available from the corresponding authors upon request. Source data are provided with this paper.

ACKNOWLEDGMENT

K.R. is grateful to the Flemish Research Foundation (FWO) for financial support under the CATCO2RE project (S004118N) and from the doctoral fellowship grant (1S94723N). T.R. and C.V. thank the Russel Berri Nanotechnology Institute for scientific research support. Henk van de Bovenkamp and Gert-Jan Boer are acknowledged for technical support.

REFERENCES

1. Bergero, C., Gosnell, G., Gielen, D., Kang, S., Bazilian, M. & Davis, S. J. Pathways to net-zero emissions from aviation. *Nat Sustain* **6**, 404–414 (2023).

2. Dray, L., Schäfer, A. W., Grobler, C., Falter, C., Allroggen, F., Stettler, M. E. J. & Barrett, S. R. H. Cost and emissions pathways towards net-zero climate impacts in aviation. *Nat Clim Chang* **12**, 956–962 (2022).

3. Viswanathan, V., Epstein, A. H., Chiang, Y. M., Takeuchi, E., Bradley, M., Langford, J. & Winter, M. The challenges and opportunities of battery-powered flight. *Nature* **601**, 519–525 (2022).

4. Vogt, E. T. C. & Weckhuysen, B. M. The refinery of the future. *Nature* **629**, 295–306 (2024).

5. Rommens, K. T. & Saeys, M. Molecular Views on Fischer-Tropsch Synthesis. *Chem Rev* **123**, 5798–5858 (2023).

6. Khodakov, A. Y., Chu, W. & Fongarland, P. Advances in the development of novel cobalt Fischer-Tropsch catalysts for synthesis of long-chain hydrocarbons and clean fuels. *Chem Rev* **107**, 1692–744 (2007).

7. Li, J., He, Y., Tan, L., Zhang, P., Peng, X., Oruganti, A., Yang, G., Abe, H., Wang, Y. & Tsubaki, N. Integrated tuneable synthesis of liquid fuels via Fischer–Tropsch technology. *Nat Catal* **1**, 787–793 (2018).

8. Voigt, C., Kleine, J., Sauer, D., Moore, R. H., Bräuer, T., Le Clercq, P., Kaufmann, S., Scheibe, M., Jurkat-Witschas, T., Aigner, M., Bauder, U., Boose, Y., Borrmann, S., Crosbie, E., Diskin, G. S., DiGangi, J., Hahn, V., *et al.* Cleaner burning aviation fuels can reduce contrail cloudiness. *Commun Earth Environ* **2**, (2021).

9. Er-Rbib, H., Bouallou, C. & Werkoff, F. Production of synthetic gasoline and diesel fuel from dry reforming of methane. *Energy Procedia* **29**, 156–165 (2012).

10. Rostrup-Nielsen, J. R. Syngas in perspective. *Catal Today* **71**, 243–247 (2002).

11. Hao, X., Djatmiko, M. E., Xu, Y., Wang, Y., Chang, J. & Li, Y. Simulation analysis of a gas-to-liquid process using aspen plus. *Chem Eng Technol* **31**, 188–196 (2008).

12. Panahi, M., Rafiee, A., Skogestad, S. & Hillestad, M. A natural gas to liquids process model for optimal operation. *Ind Eng Chem Res* **51**, 425–433 (2012).

13. Ermolaev, I. S., Ermolaev, V. S. & Mordkovich, V. Z. Efficiency of gas-to-liquids technology with different synthesis gas production methods. *Ind Eng Chem Res* **53**, 2758–2763 (2014).

14. Adelung, S., Maier, S. & Dietrich, R. U. Impact of the reverse water-gas shift operating conditions on the Power-to-Liquid process efficiency. *Sustainable Energy Technologies and Assessments* **43**, (2021).

15. König, D. H., Baucks, N., Dietrich, R. U. & Wörner, A. Simulation and evaluation of a process concept for the generation of synthetic fuel from CO_2 and H_2. *Energy* **91**, 833–841 (2015).

16. Uribe-Soto, W., Portha, J. F., Commenge, J. M. & Falk, L. A review of thermochemical processes and technologies to use steelworks off-gases. *Renewable and Sustainable Energy Reviews* **74**, 809–823 (2017).

17. Savost'yanov, A. P., Yakovenko, R. E., Narochnyi, G. B. & Lapidus, A. L. Effect of the dilution of synthesis gas with nitrogen on the Fischer–Tropsch process for the production of hydrocarbons. *Solid Fuel Chemistry* **49**, 356–359 (2015).

18. Muleja, A. A., Yao, Y., Glasser, D. & Hildebrandt, D. Effect of feeding nitrogen to a fixed bed Fischer-Tropsch reactor while keeping the partial pressures of reactants the same. *Chemical Engineering Journal* **293**, 151–160 (2016).

19. Jess, A., Popp, R. & Hedden, K. Fischer-Tropsch-synthesis with nitrogen-rich syngas Fundamentals and reactor design aspects. *Appl Catal A Gen* **186**, 321–342 (1999).

20. Khodakov, A. Y., Chu, W. & Fongarland, P. Advances in the development of novel cobalt Fischer-Tropsch catalysts for synthesis of long-chain hydrocarbons and clean fuels. *Chem Rev* **107**, 1692–1744 (2007).

21. Scarfiello, C., Pham Minh, D., Soulantica, K. & Serp, P. Oxide Supported Cobalt Catalysts for CO_2 Hydrogenation to Hydrocarbons: Recent Progress. *Adv Mater Interfaces* **10**, (2023).

22. Suo, Y., Yao, Y., Zhang, Y., Xing, S. & Yuan, Z. Y. Recent advances in cobalt-based Fischer-Tropsch synthesis catalysts. *Journal of Industrial and Engineering Chemistry* **115**, 92–119 (2022).

23. Zhang, Y., Jacobs, G., Sparks, D. E., Dry, M. E. & Davis, B. H. CO and CO_2 hydrogenation study on supported cobalt Fischer-Tropsch synthesis catalysts. *Catal Today* **71**, 411–418 (2002).

24. Riedel, T. & Schaub, G. Low-temperature Fischer-Tropsch synthesis on cobalt catalysts-effects of CO_2. *Topics in Catalysis* **26**, 145–155 (2003).

25. Gnanamani, M. K., Shafer, W. D., Sparks, D. E. & Davis, B. H. Fischer-Tropsch synthesis: Effect of CO_2 containing syngas over Pt promoted Co/γ-Al_2O_3 and K-promoted Fe catalysts. *Catal Commun* **12**, 936–939 (2011).

26. Díaz, J. A., De La Osa, A. R., Sánchez, P., Romero, A. & Valverde, J. L. Influence of CO_2 co-feeding on Fischer-Tropsch fuels production over carbon nanofibers supported cobalt catalyst. *Catal Commun* **44**, 57–61 (2014).

27. Riedel, T., Claeys, M., Schulz, H., Schaub, G., Nam, S. S., Jun, K. W., Choi, M. J., Kishan, G. & Lee, K. W. Comparative study of Fischer-Tropsch synthesis with H_2/CO and H_2/CO_2 syngas using Fe- and Co-based catalysts. *Appl Catal A Gen* **186**, 201–213 (1999).

28. Yao, Y., Hildebrandt, D., Glasser, D. & Liu, X. Fischer-Tropsch synthesis using H_2/CO/CO_2 syngas mixtures over a cobalt catalyst. *Ind Eng Chem Res* **49**, 11061–11066 (2010).

29. Chakrabarti, D., De Klerk, A., Prasad, V., Gnanamani, M. K., Shafer, W. D., Jacobs, G., Sparks, D. E. & Davis, B. H. Conversion of CO_2 over a Co-based Fischer-Tropsch catalyst. *Ind Eng Chem Res* **54**, 1189–1196 (2015).

30. Visconti, C. G., Lietti, L., Tronconi, E., Forzatti, P., Zennaro, R. & Finocchio, E. Fischer-Tropsch synthesis on a Co/Al_2O_3 catalyst with CO_2 containing syngas. *Appl Catal A Gen* **355**, 61–68 (2009).

31. Guilera, J., Díaz-López, J. A., Berenguer, A., Biset-Peiró, M. & Andreu, T. Fischer-Tropsch synthesis: Towards a highly-selective catalyst by lanthanide promotion under relevant CO_2 syngas mixtures. *Appl Catal A Gen* **629**, (2022).

32. Hong, G. H. & Moon, D. J. Development of fixed bed reactor for application in GTL-FPSO: The effect of nitrogen and carbon dioxide contents in feed gas on Fischer-Tropsch synthesis reaction over Ru/Co/Al_2O_3 catalyst. *Catal Today* **353**, 73–81 (2020).

33. Daramola, M. O., Matamela, K. & Sadare, O. O. Effect of CO_2 co-feeding on the conversion of syngas derived from waste to liquid fuel over a bi-functional Co/H-ZSM-5 catalyst. *J Environ Chem Eng* **5**, 54–62 (2017).

613 34. Park, K. S., Saravanan, K., Park, S.-J., Lee, Y.-J., Jeon, K.-W. & Bae, J. W. Effects of CO_2
614 to deactivation behaviors of Co/Al_2O_3 and Co/SiO_2 for CO hydrogenation to hydrocarbons. *Catal.*
615 *Sci. Technol.* **7**, 4079–4091 (2017).

616 35. González-Castaño, M., Dorneanu, B. & Arellano-García, H. The reverse water gas shift
617 reaction: A process systems engineering perspective. *React Chem Eng* **6**, 954–976 (2021).

618 36. van Koppen, L. M., Dugulan, A. I., Leendert Bezemer, G. L. & Hensen, E. J. M.
619 Elucidating deactivation of titania-supported cobalt Fischer-Tropsch catalysts under simulated
620 high conversion conditions. *J Catal* **420**, 44–57 (2023).

621 37. van Koppen, L. M., Dugulan, A. I., Hensen, E. J. M. & Bezemer, G. L. Tuning stability of
622 titania-supported Fischer-Tropsch catalysts: Impact of surface area and noble metal promotion.
623 *Catal Today* **429**, (2024).

624 38. Le, T. A., Kim, M. S., Lee, S. H. & Park, E. D. CO and CO_2 Methanation Over Supported
625 Cobalt Catalysts. *Top Catal* **60**, 714–720 (2017).

626 39. Ten Have, I. C., Kromwijk, J. J. G., Monai, M., Sterk, E. B., Meirer, F. & Weckhuysen, B.
627 M. Uncovering the reaction mechanism behind CoO as active phase for CO_2 hydrogenation. *Nat*
628 *Commun* **13**, (2022).

629 40. Melaet, G., Ralston, W. T., Li, C. S., Alayoglu, S., An, K., Musselwhite, N., Kalkan, B. &
630 Somorjai, G. A. Evidence of highly active cobalt oxide catalyst for the Fischer-Tropsch synthesis
631 and CO_2 hydrogenation. *J Am Chem Soc* **136**, 2260–2263 (2014).

632 41. Eschemann, T. O., Oenema, J. & De Jong, K. P. Effects of noble metal promotion for
633 Co/TiO_2 Fischer-Tropsch catalysts. *Catal Today* **261**, 60–66 (2016).

634 42. Hernández Mejía, C., van Deelen, T. W. & de Jong, K. P. Activity enhancement of cobalt
635 catalysts by tuning metal-support interactions. *Nat Commun* **9**, (2018).

636 43. Muleja, A. A., Yao, Y., Glasser, D. & Hildebrandt, D. Effect of feeding nitrogen to a fixed
637 bed Fischer-Tropsch reactor while keeping the partial pressures of reactants the same. *Chemical*
638 *Engineering Journal* **293**, 151–160 (2016).

639 44. Eschemann, T. O., Oenema, J. & De Jong, K. P. Effects of noble metal promotion for
640 Co/TiO_2 Fischer-Tropsch catalysts. *Catal Today* **261**, 60–66 (2016).

641 45. Hernández Mejía, C., van Deelen, T. W. & de Jong, K. P. Activity enhancement of cobalt
642 catalysts by tuning metal-support interactions. *Nat Commun* **9**, (2018).

643 46. Bezemer, G. L., Bitter, J. H., Kuipers, H. P. C. E., Oosterbeek, H., Holewijn, J. E., Xu, X.,
644 Kapteijn, F., Van Diilen, A. J. & De Jong, K. P. Cobalt particle size effects in the Fischer-Tropsch
645 reaction studied with carbon nanofiber supported catalysts. *J Am Chem Soc* **128**, 3956–3964
646 (2006).

647 47. Li, W., Nie, X., Yang, H., Wang, X., Polo-Garzon, F., Wu, Z., Zhu, J., Wang, J., Liu, Y.,
648 Shi, C., Song, C. & Guo, X. Crystallographic dependence of CO_2 hydrogenation pathways over
649 HCP-Co and FCC-Co catalysts. *Appl Catal B* **315**, (2022).

48. Song, D., Li, J. & Cai, Q. In situ diffuse reflectance FTIR study of CO adsorbed on a cobalt catalyst supported by silica with different pore sizes. *Journal of Physical Chemistry C* **111**, 18970–18979 (2007).

49. Paredes-Nunez, A., Lorito, D., Burel, L., Motta-Meira, D., Agostini, G., Guilhaume, N., Schuurman, Y. & Meunier, F. CO Hydrogenation on Cobalt-Based Catalysts: Tin Poisoning Unravels CO in Hollow Sites as a Main Surface Intermediate. *Angewandte Chemie int. ed.* **130**, 556–559 (2018).

50. Chen, W., Zijlstra, B., Filot, I. A. W., Pestman, R. & Hensen, E. J. M. Mechanism of Carbon Monoxide Dissociation on a Cobalt Fischer–Tropsch Catalyst. *ChemCatChem* **10**, 136–140 (2018).

51. Weststrate, C. J., van de Loosdrecht, J. & Niemantsverdriet, J. W. Spectroscopic insights into cobalt-catalyzed Fischer-Tropsch synthesis: A review of the carbon monoxide interaction with single crystalline surfaces of cobalt. *J Catal* **342**, 1–16 (2016).

52. Zennaro, R., Tagliabue, M. & Bartholomew, C. H. Kinetics of Fischer-Tropsch synthesis on titania-supported cobalt. *Catal Today* **58**, 309–319 (2000).

53. Rommens, K. T., Gunasooriya, G. T. K. K. & Saeys, M. Key Role of CO Coverage for Chain Growth in Co-Based Fischer-Tropsch Synthesis. *ACS Catalysis* **14**, 6696–6709 (2024).

54. Gunasooriya, G. T. K. K., Van Bavel, A. P., Kuipers, H. P. C. E. & Saeys, M. CO adsorption on cobalt: Prediction of stable surface phases. *Surf Sci* **642**, L6–L10 (2015).

55. Zhang, M., Wang, M., Xu, B. & Ma, D. How to Measure the Reaction Performance of Heterogeneous Catalytic Reactions Reliably. *Joule* **3**, 2876–2883 (2019).

56. Kresse, G. & Hafner, J. Ab initio molecular dynamics for liquid metals. *Phys. Rev. B* **47**, (1993).

57. Kresse, G. & Furthmüller, J. Efficiency of ab-initio total energy calculations for metals and semiconductors using a plane-wave basis set. *Comput Mater Sci* **6**, 15–50 (1996).

58. Kresse, G. & Furthmüller, J. Efficient iterative schemes for ab initio total-energy calculations using a plane-wave basis set. *Phys. Rev. B* **54**, (1996).

59. Klimeš, J., Bowler, D. R. & Michaelides, A. Chemical accuracy for the van der Waals density functional. *Journal of Physics Condensed Matter* **22**, (2010).

60. Klimeš, J., Bowler, D. R. & Michaelides, A. Van der Waals density functionals applied to solids. *Phys Rev B Condens Matter Mater Phys* **83**, (2011).

61. Coltrin, M. E., Kee, R. J., Rupley, F. M. & Meeks, E. Surface Chemkin-III: A Fortran Package for Analyzing Heterogeneous Chemical Kinetics at a Solid-Surface-Gas-Phase Interface. (1996).

62. Li, S. & Petzold, L. Software and algorithms for sensitivity analysis of large-scale differential algebraic systems. *J Comput Appl Math* **125**, 131–145 (2000).

63. Rommens, K. T., Gunasooriya, G. T. K. K. & Saeys, M. Supplementary Data and Microkinetic Model for 'Key Role of CO Coverage for Chain Growth in Co-Based Fischer-Tropsch Synthesis'. *Zenodo* (2024).

64. Bak, K. L., Jørgensen, P., Olsen, J., Helgaker, T. & Klopper, W. Accuracy of atomization energies and reaction enthalpies in standard and extrapolated electronic wave function/basis set calculations. *Journal of Chemical Physics* **112**, 9229–9242 (2000).

65. Saeys, M., Reyniers, M. F., Neurock, M. & Marin, G. B. Ab initio reaction path analysis of benzene hydrogenation to cyclohexane on Pt(111). *Journal of Physical Chemistry B* **109**, 2064–2073 (2005).

66. Cheula, R., Tran, T. A. M. Q. & Andersen, M. Unraveling the Effect of Dopants in Zirconia-Based Catalysts for CO_2 Hydrogenation to Methanol. *ACS Catal* **14**, 13126–13135 (2024).

67. Christensen, R., Hansen, H. A. & Vegge, T. Identifying systematic DFT errors in catalytic reactions. *Catal Sci Technol* **5**, 4946–4949 (2015).

68. Saeys, M., Reyniers, M. F., Neurock, M. & Marin, G. B. Density functional theory analysis of benzene (De)hydrogenation on Pt(111): Addition and removal of the first two H-atoms. *Journal of Physical Chemistry B* **107**, 3844–3855 (2003).

705 Graphical Abstract:

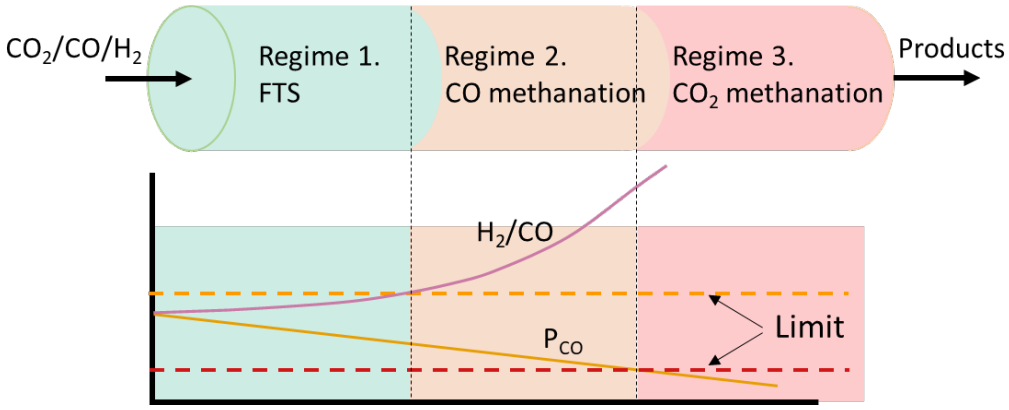

706

707

708